

Realism Control One-step Diffusion for Real-World Image Super-Resolution

Zongliang Wu^{1, 2, 3, *}, Siming Zheng^{3, *}, Peng-Tao Jiang^{3, #}, Xin Yuan^{2, #}

¹ Zhejiang University, Hangzhou, China

² School of Engineering, Westlake University, Hangzhou, China

³ vivo Mobile Communication Co., Ltd

* Equal Contribution # Corresponding Author

{wuzongliang, xyuan}@westlake.edu.cn, {zhengsiming, pt.jiang}@vivo.com

Abstract

Pre-trained diffusion models have shown great potential in real-world image super-resolution (Real-ISR) tasks by enabling high-resolution reconstructions. While one-step diffusion (OSD) methods significantly improve efficiency compared to traditional multi-step approaches, they still have limitations in balancing fidelity and realism across diverse scenarios. Since the OSDs for SR are usually trained or distilled by a single timestep, they lack flexible control mechanisms to adaptively prioritize these competing objectives, which are inherently manageable in multi-step methods through adjusting sampling steps. To address this challenge, we propose a Realism Controlled One-step Diffusion (RCOD) framework for Real-ISR. RCOD provides a latent domain grouping strategy that enables explicit control over fidelity-realism trade-offs during the noise prediction phase with minimal training paradigm modifications and original training data. A degradation-aware sampling strategy is also introduced to align distillation regularization with the grouping strategy and enhance the controlling of trade-offs. Moreover, a visual prompt injection module is used to replace conventional text prompts with degradation-aware visual tokens, enhancing both restoration accuracy and semantic consistency. Our method achieves superior fidelity and perceptual quality while maintaining computational efficiency. Extensive experiments demonstrate that RCOD outperforms state-of-the-art OSD methods quantitatively and visually, with flexible realism control capabilities in the inference stage. Code is available at <https://zongliang-wu.github.io/RCOD-SR>.

Introduction

Image super-resolution (SR) (Dong et al. 2015; Zhang et al. 2018b, 2021; Ledig et al. 2017; Liang et al. 2021) aims to recover a high-resolution (HR) image from its low-resolution (LR) counterpart.

Traditional image super-resolution simplifies the degradation process as known noise, blur, or downsampling. In recent years, real-world image super-resolution (Real-ISR) (Zhang et al. 2021; Wang et al. 2021) has attracted more attention due to the increasing demand for reconstructing high-resolution images under real-world unknown degradations, which is more challenging and practical in real applications.

Copyright © 2026, Association for the Advancement of Artificial Intelligence (www.aaai.org). All rights reserved.



Figure S1: While previous one-step diffusion methods, such as S3Diff (Zhang et al. 2024) only yield one optimal result (b), our approach offers the flexibility to control images (c-d) with different fidelity-realism trade-offs during inference, enhancing practical applicability across different scenarios.

While recent advances in Stable Diffusion (SD) models (Ho, Jain, and Abbeel 2020; Song et al. 2020), especially the large-scale pretrained text-to-image (T2I) models have demonstrated unprecedented capabilities in various downstream vision tasks (Zhang, Rao, and Agrawala 2023; Rombach et al. 2022). Some works leveraging pre-trained SD models for multi-step SR, such as DiffBIR (Lin et al. 2023), StableSR (Wang et al. 2024a), and SeeSR (Wu et al. 2024b), have achieved remarkable SR quality through iterative latent space optimization. Though these methods achieve impressive perceptual quality, they suffer from computational inefficiency. The caused latency by multi-step sampling makes real-time applications impractical.

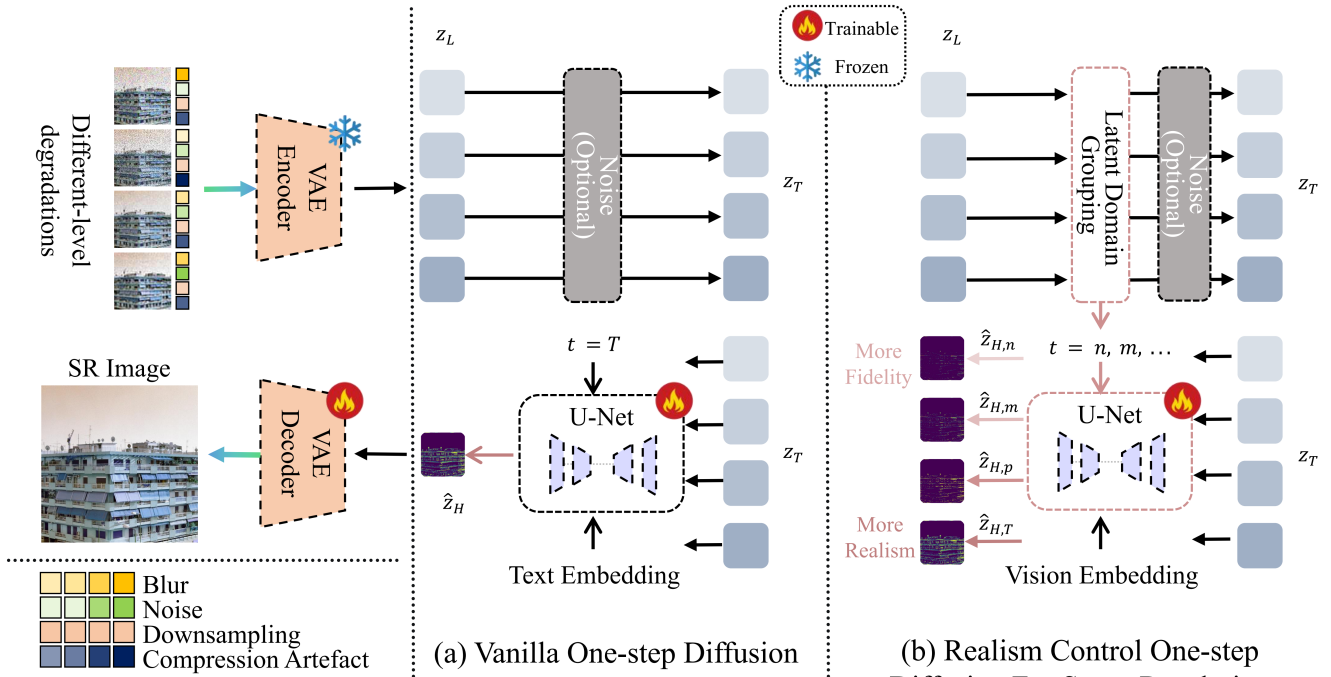


Figure S2: Realism control one-step diffusion (RCOD) training process. The left part illustrates several synthesized real-world LR images by applying diverse degradations with varying types and intensities on an HR image. (a) Existing vanilla one-step diffusion (OSD) methods for super-resolution (SR): These LR images are directly sent into the diffusion forward and reverse process; the denoising U-Net tends to learn to recover the ‘average’ degradation, leading to a monotonous generation ability within the latent domain. (b) Our proposed Realism Control One-Step Diffusion employs a latent domain grouping strategy. This allows for adaptive control of timesteps (denoising degrees) during the forward process according to the degradation degree in the latent domain. As a result, the denoising U-Net can acquire a more diverse generation capability based on the timestep.

To address the efficiency concerns, recent attempts focus on one-step diffusion frameworks (Wu et al. 2024a; Zhang et al. 2024), which distill multi-step diffusion priors into single-step inference through knowledge distillation and achieve 10x to 100x speedup over previous multi-step diffusion-based SR methods. However, existing one-step diffusion approaches face a fundamental dilemma: the deterministic single-step generation inherently lacks the controllable fidelity-realism balance that multi-step methods achieve via step-wise noise scheduling. As illustrated in Fig. S1, previous one-step diffusion super-resolution (SR) methods, such as S3Diff (Zhang et al. 2024), can only generate a single optimal result but can not meet the need for dynamic adjustment between fidelity and realism. The root cause lies in current OSD training paradigms. Most methods align all the LR inputs under different unknown degradations with a single convergence space through single timestep conditioned training, which results in a balanced static preference for fidelity or realism and prevents adaptive adjustments for scenario-specific requirements.

Bearing the above concerns in mind, we propose a novel framework that provides one-step diffusion Real-ISR methods with the capability to monotonically control the level of realism. This framework, which we denote as **Realism Controlled One-step Diffusion (RCOD)**, can be easily integrated into existing one-step diffusion methods for Real-

ISR. Specifically, during the training phase, we incorporate a Latent Domain Grouping (LDG) strategy into the latent diffusion process, grouping training data according to a latent domain metric. Through this strategy, the diffusion denoising network learns to perceive variations in degradation across training samples, thereby gaining adaptive restoration capabilities. Furthermore, to address the inherent limitations caused by text prompts, we introduce a Visual Prompt Injection Module (VPIM) to enhance prompt quality. Our contributions are summarized as follows:

- We propose a simple but effective latent domain grouping (LDG) strategy that reformulates the noise prediction process by partitioning the latent space into fidelity and realism oriented domains. This allows explicit control over detail preservation versus generative enhancement through simple training paradigm modifications, without requiring additional trainable parameters.
- During distillation, we introduce a degradation-aware sampling (DAS) strategy that reformulates timestep sampling in the pretrained model by adaptively aligning it with our LDG framework, enhancing controlling with regularization strength.
- To reduce the computational burden of VLM and dependencies on manual text prompts, we propose a visual prompt injection module (VPIM) to replace text prompts

with degradation-aware visual tokens, enhancing both restoration accuracy and semantic consistency.

- We empirically evaluate our approach on widely used stable diffusion-based and their distillation version Real-ISR methods, demonstrating quality improvement and the effectiveness of proposed approach.

Related Work

Real-World Image Super-Resolution

To address the challenge of recovering real-world low-resolution (LR) observations with unknown degradations, the Real-ISR task has been introduced. Due to the complex degradations involved, Real-ISR has been a challenging problem for some time (Ignatov et al. 2017; Liu et al. 2022; Ji et al. 2020). Initial methods trained their models with simple downsampling techniques (Kim, Kwon Lee, and Mu Lee 2016; Zhang et al. 2018b), which led to poor performance on real-world datasets. BSRGAN (Zhang et al. 2021) and Real-ESRGAN (Wang et al. 2021) were among the first to introduce a more realistic synthesis pipeline for LR images, enabling deep learning methods to be applied to real-world scenarios. However, these GAN-based methods often suffer from artifacts and training instability. With the emergence of the powerful pre-trained text-to-image generation model Stable Diffusion (SD) (Rombach et al. 2022), many efforts have been made to leverage its strong generative capabilities for solving the Real-ISR problem, such as DiffBIR (Lin et al. 2023), StableSR (Wang et al. 2024a) and SeeSR (Wu et al. 2024b), and FaithDiff (Chen, Pan, and Dong 2025). These SD-based methods improve fidelity and perceptual quality, but their application is limited due to the significant computational resources and time required. This is primarily due to the dozens to hundreds of timesteps involved in the diffusion denoising process.

One-step Diffusion Models for Real-ISR

To reduce the computational cost during inference, one-step diffusion methods have been proposed. These methods utilize model distillation techniques specifically designed for diffusion models, including progressive distillation (Meng et al. 2023; Salimans and Ho 2022), consistency models (Song et al. 2023), distribution matching distillation (Yin et al. 2024b,a), and variational score distillation (VSD) (Wang et al. 2024c; Nguyen and Tran 2024). In the context of Real-ISR, OSEDiff (Wu et al. 2024a) employs the VSD strategy to achieve one-step diffusion based on a pre-trained SD model. Similarly, S3Diff (Zhang et al. 2024) directly employs a distilled Stable Diffusion Turbo (SD-T) model for Real-ISR. Recent works including ADCSR (Chen et al. 2025) and TSD-SR (Dong et al. 2025) also improve OSD performance and efficiency. InvSR (Yue, Liao, and Loy 2025) offers a flexible sampling mechanism with arbitrary-steps (1-5) diffusion.

However, while time efficiency is improved, another dilemma arises: one-step diffusion methods struggle to generate diverse outputs balancing fidelity and realism—a critical requirement for real-world applications—unlike multi-step approaches that achieve this through progressive noise

scheduling. In other words, current one-step diffusion methods for Real-ISR cannot control fidelity and realism as effectively as their multi-step counterparts. Some techniques, such as ControlNet models (Zhang, Rao, and Agrawala 2023), can enhance HR image generation by controlling semantic content but cannot achieve pixel-level control and require additional conditions, such as extra images or depth maps. Therefore, these techniques cannot be directly employed in one-step diffusion methods for Real-ISR. OFTSR (Zhu et al. 2024) achieves fidelity trade-offs through trajectory alignment distillation, but lacks degradation-aware mechanisms for real-world scenarios. PiSA-SR (Sun et al. 2025) controls fidelity and realism by training and inference with two different LoRA (Hu et al. 2022) modules and two-step diffusion, which obviously increases the computational cost compared to using a single step. Thus, a simple, efficient, and generalizable method for fidelity-realism control in OSD for Real-ISR remains essential.

Methodology

In this section, we first reveal the characteristic of denoising network in one-step diffusion for image super-resolution, and then propose our algorithm.

Preliminary: The Character of Denoising Network in One-step Diffusion for Real-ISR

In SD, the latent diffusion process starts with encoding an image into a latent representation z_0 using a VAE encoder. The forward diffusion process then adds Gaussian noise to z_0 over T steps via a Markov chain defined as:

$$q(z_t|z_{t-1}) = \mathcal{N}(z_t; \sqrt{1 - \beta_t}z_{t-1}, \beta_t\mathcal{I}) \quad (1)$$

following a variance schedule β_1, \dots, β_T . Here $z_0 \sim q(z_0)$. The forward process is: $z_t = \alpha_t z_0 + \sigma_t \epsilon$, where $\alpha_t = \prod_{s=1}^t \sqrt{1 - \beta_s}$, $\sigma_t = \sqrt{1 - \alpha_t^2}$, and $\epsilon \sim \mathcal{N}(\mathbf{0}, \mathcal{I})$. Here, the mean of z_t becomes $\alpha_t z_0$, and the variance is $\sigma_t^2 \mathcal{I}$. With larger t , more noise is added, resulting in a greater deviation of the mean (scaled by $\alpha_t < 1$) and an increased variance (σ_t^2), distancing z_t from the original distribution z_0 .

The reverse process denoises z_t to recover z_{t-1} :

$$p_\theta(z_{t-1}|z_t) = \mathcal{N}(z_{t-1}; \mu_\theta(z_t, t), \Sigma_\theta(z_t, t)), \quad (2)$$

where a time-conditional U-Net ϵ_θ predicts the noise ϵ to estimate μ_θ and Σ_θ . Multi-step diffusion models iteratively refine z_T back to z_0 over T steps, while one-step diffusion methods, often distilled from multi-step models, predict the clean data directly from z_T in a single step, significantly reducing computation.

For Real-ISR tasks using SD-based OSD methods like (Wu et al. 2024a), the process from LR latent features z_L to HR latent features \hat{z}_H is formulated as a one-step denoising process:

$$\hat{z}_H = F_\theta(z_L; T, c_y) \triangleq \frac{z_L - \beta_T \epsilon_\theta(z_L; T, c_y)}{\alpha_T}, \quad (3)$$

where z_L is the LR latent representation, c_y is the text embedding, and ϵ_θ is the denoising network predicting noise at

timestep T . As shown in Fig. S2(a), vanilla OSD methods learn a direct latent feature mapping from LR to HR images with or without adding additional noise.

In Real-ISR, images exhibit diverse degradation types and levels. SD-based methods use powerful generative image priors to recover LR images. However, OSD typically trains on all data with a fixed timestep T with a constant noise level. This results in a model that generates a uniform amount of detail and converges to a confined domain, which may not suit images with varying degradation severity. Tab. S1 (a) demonstrates the results of training OSEDiff on two different degradation pipelines (DP). ‘Orig.+ New Deg.’ denotes a DP applying more degradations than the standard DP (‘Orig.’). It indicates that higher degradation in training results in a greater emphasis on realism. This exposes OSD’s flaw: by locking training to a single fixed T , the model optimizes for an “**average**” degradation, yielding a limited generation flexibility that struggles to adapt its output to meet the specific scenario requirements.

In contrast, multi-step diffusion models provide greater flexibility in SR tasks. By selecting different timesteps t during the inference stage, these models control the degree of noise adding and removing in diffusion, balancing fidelity and realism effectively.

Therefore, to overcome the inherent limitation of OSD, which is incapable of adjusting its generation levels to adapt to varying scenarios, we propose a novel training strategy for real-world SR applications that can flexibly control the generation realism during the inference stage.

Metrics	Orig.	Orig.+New Deg.	M_L	L1	MSE	Cosine Sim.
PSNR \uparrow	25.15	24.59	SSIM \uparrow	0.60	0.54	0.78
MANIQA \uparrow	0.6326	0.6462	DISTS \uparrow	0.15	0.11	0.42
			CLIPIQA \uparrow	0.06	0.05	0.27

(a)

(b)

Table S1: (a) Influence of degradation degree in training data. (b) |Spearman coefficient| \uparrow comparison of different M_L distances and image quality metrics.

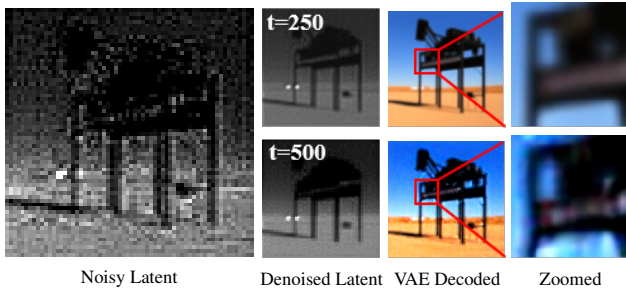


Figure S3: Influence of different timesteps t using SD-turbo.

Latent Domain Grouping

To achieve dynamic fidelity-realism trade-offs control in OSD generated SR results, we focus on the most basic condition in denoising network, *i.e.*, timestep condition. Unlike

prompts from a text encoder or a vision encoder, the timestep condition is an unremovable component in the diffusion process. At the same time, it controls the mean and variance of noisy latent feature z_T . With the larger mean and variance difference between z_T and z_0 , more contents will be generated during the denoising process. Fig. S3 shows an example of influence of different t . In the foundational model SD-turbo, the higher timestep value during the diffusion process usually reflects the the higher capability generating.

Therefore, to easily control the generation degree, we propose a latent domain grouping (LDG) strategy. Recall Eq. (3), we do not use a single fixed timestep T , but choose a timestep t according to a metrics:

$$\hat{z}_H = F_\theta(z_L; t, c_y), \quad (4)$$

$$t = k \cdot \left(n - \left\lfloor \frac{n \cdot (M_L - M_{L-\min})}{(M_{L-\max} - M_{L-\min})} \right\rfloor \right), k \in \mathbb{Z}^+, \quad (5)$$

where M_L denotes a latent metric that can perceive the “level of degradation” of features in latent domain, $M_{L-\min}$ is the minimum value of M_L in training data, k is interval of timestep, $\lfloor \cdot \rfloor$ denotes the maximum integer no larger than the entry inside, n is number of groups for timestep.

To employ this strategy both on SD and distillation version of SD, *i.e.*, SD-Turbo (SDT), which distilled a four specific steps from the original 1000-step diffusion process, we set n to be ≤ 4 and $k = 250$.

By the grouping strategy, denoising network can learn different degrees of generation according to timestep. In the training stage, grouping is based on the M_L described in the next subsection. In the inference stage, we can easily choose a timestep to control the level of realism for SR in different scenarios. Furthermore, due to our grouping strategy, the realism level increases monotonically with the timestep.

Latent Metric for Denoising Network

The latent metric M_L is designed to enable the denoising network in the latent domain to perceive the “level of degradation” of the low-resolution features z_L . Here, we define the “level of degradation” as the extent to which z_L deviates from its HR counterpart z_H . Thus, the definition of the latent metric M_L should reflect the characteristics of z_L that indicate this degradation.

A simple choice might be to use the difference between the mean values of z_L and z_H , as the forward diffusion process scales the mean of z_L over time. However, as shown in Fig. S4(a), the mean values of z_L and z_H are similar across the training data. This suggests that mean difference fails to effectively capture the degradation level.

Instead, we use cosine similarity (CS) as M_L :

$$M_L = \frac{z_L \cdot z_H}{\|z_L\| \|z_H\|}. \quad (6)$$

Cosine similarity is a widely adopted measure in representation learning (e.g., contrastive learning (Chen et al. 2020)). It can quantify the divergence between high-dimensional latent features z_L and z_H , which can reflect high-level changes caused by degradation. As shown in Fig. S4(b), most cosine similarity values lie between 0 and 1, providing

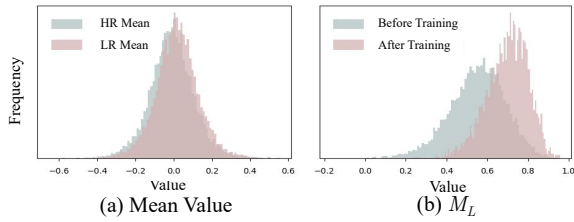


Figure S4: Distribution of (a) mean value of LR and HR training images in the latent domain, (b) the M_L metric in the latent domain of VAE before and after training.

a clear range to distinguish varying degrees of degradation for the denoising network.

Different distances inherently introduce a certain preference or bias, to evaluate the bias of different M_L , we calculate correlation coefficient ($|\text{Spearman Corr.}| \uparrow$) of CS, L1, and MSE with different metrics in Table S1 (b). The metrics are calculated between LR and HR images. The correlation reflects the degree of association between various M_L and different metrics. CS exhibits a higher correlation coefficient with objective (SSIM), perceptual (DISTS), and semantic (CLIPQA) metrics compared to other distances in latent space. **More visualization results can be seen in Supplementary Materials (SM).**

Metric Estimation

Since \mathbf{z}_H is introduced as a latent metric, we can only calculate it during training. In the inference stage, beyond manually choosing a timestep, we also consider an adaptive timestep selection, i.e., estimating an M_L for each LR image. Benefiting from the powerful representation ability of the pre-trained model, we use features from intermediate layers as input and a simple MLP as a metric estimation module (MEM), operating independently of OSD training.

Degradation-aware Sampling Distillation

Previous VSD method for SR (Wu et al. 2024a), utilizes the regularization network (a pre-trained SD) that sampled timesteps across a wide range (20-980). This aims to generate regularization latent features and, in turn, optimize the distribution of the OSD network. However, to better integrate the distillation process with the concept of degradation in the latent space, we propose a Degradation-Aware Sampling (DAS) strategy. DAS redefines how timesteps are sampled in the pre-trained model, adaptively aligning this process with our LDG framework to provide explicit control over regularization strength. The DAS can be written as:

$$t_r = S(\max(20, t - k), \min(980, t + k)) \quad (7)$$

where t_r is the sample timestep for regularization network, t is the chosen timestep in OSD network by LDG, $S(t_{min}, t_{max})$ denotes uniformly random sampling of an integer from the range $[t_{min}, t_{max}]$.

By applying DAS, the degradation grouping information is delivered from LDG, thereby aligning this process with LDG and control over regularization strength.

Visual Prompt Injection Module

In previous SD-based super-resolution (SR) methods like OSediff (Wu et al. 2024a) and SeeSR (Wu et al. 2024b), text encoders, sometimes paired with a vision-language model (VLM) as a text prompt extractor, improve non-reference (NR) metrics, which assess realism, but often constrain full-reference (FR) metrics, which assess fidelity to the ground truth. This trade-off arises because text prompts provide high-level semantic guidance to enhance realism, yet they may compromise structural accuracy.

LR feature \mathbf{z}_L solely from the VAE encoder offers limited semantic information. Without additional context, the conditioned U-Net struggles to generate high-quality outputs. Text prompts attempt to bridge this gap by injecting external semantic cues, but they come with drawbacks: VLMs increase computational costs, and the prompts may not fully align with the image’s content. Some methods like S3Diff (Zhang et al. 2024) use fixed text to reduce complexity, yet still struggle to balance NR and FR metrics.

To address these issues, we propose the Visual Prompt Injection Module (VPIM), which replaces conventional text prompts with degradation-aware visual tokens. VPIM substitutes the text encoder (typically a CLIP text model) with a CLIP vision model and an MLP layer for dimension alignment. The LR image serves as its input, i.e., visual prompt, and the output is fed into the cross-attention of the U-Net. By adopting VPIM, we eliminate the need for VLMs, reduce computational overhead, and provide the U-Net with image-specific semantic information directly from the LR input. The visual prompt is tied to the image’s pixel characteristics, leading to improvement in both fidelity and realism.

With the combination of LDG, latent metric, DAS, and VPIM, we proposed a Realism control one-step diffusion (RCOD) framework, a realism-flexible one-step diffusion model with enhanced performance that can be applied to various recent mainstream one-step diffusion Real-ISR methods, thereby improving their capabilities. **We provide a pseudo-code example of our RCOD in SM.**

Experiments

Experiments Setups

Datasets: Following the training and testing settings of prior works (Wu et al. 2024b,a; Zhang et al. 2024), we employ LSDIR (Li et al. 2023) and the first 10K face images from FFHQ (Karras, Laine, and Aila 2019) for training and degradation pipeline of Real-ESRGAN (Wang et al. 2021) for LR image synthesizing. The synthetic test data use cropped 512×512 synthetic data from DIV2K-Val (Agustsson and Timofte 2017) and degraded using the Real-ESRGAN pipeline (Wang et al. 2021). The real-world data include LR-HR pairs from RealSR (Cai et al. 2019) and DRealSR (Wei et al. 2020), both with sizes of 128×128 - 512×512 for LR-HR pairs.

Evaluation Metrics: We employ widely used FR and NR metrics. FR metrics include PSNR, SSIM (Wang et al. 2004), LPIPS (Zhang et al. 2018a), and DISTS (Ding et al. 2020). NR metrics include NIQE (Zhang, Zhang, and Bovik

Datasets	Methods	PSNR \uparrow	SSIM \uparrow	LPIPS \downarrow	DISTS \downarrow	NIQE \downarrow	MUSIQ \uparrow	MANIQA \uparrow	CLIQQA \uparrow	FID \downarrow
DrealSR	SinSR	<u>28.36</u>	0.7515	0.3665	0.2485	6.991	55.33	0.4884	0.6383	170.57
	PiSA-SR	28.31	0.7804	0.2960	0.2169	6.200	66.11	0.6156	0.6970	130.61
	TSD-SR	25.67	0.7132	0.3538	0.2459	5.991	65.99	0.6327	0.7137	171.36
	InvSR	28.33	0.7502	0.3678	0.2481	6.941	55.27	0.4900	0.6385	170.57
	OSEDiff	27.92	<u>0.7835</u>	<u>0.2968</u>	0.2165	6.490	64.65	0.5899	0.6963	135.30
	RCOD _O -Fid.	28.90	0.7906	0.2919	0.2186	6.817	66.72	0.6275	0.7023	131.52
	RCOD _O -Neu.	28.30	0.7775	0.3080	0.2306	6.469	<u>68.03</u>	0.6385	0.7179	139.92
	RCOD _O -Real.	27.59	0.7600	0.3389	0.2499	6.172	68.19	0.6295	0.7325	158.16
	S3Diff	27.54	0.7491	0.3109	0.2099	6.212	63.94	0.6134	0.7130	118.64
	RCOD _S -Fid.	28.09	0.7800	0.3002	<u>0.2149</u>	5.871	65.74	0.6174	0.6963	136.62
	RCOD _S -Neu.	27.48	0.7526	0.3256	<u>0.2251</u>	<u>5.636</u>	67.40	<u>0.6339</u>	<u>0.7278</u>	138.87
	RCOD _S -Real.	26.95	0.7190	0.3607	0.2414	5.448	67.58	<u>0.6317</u>	0.7478	145.36
RCOD _S -Adap.	27.83	0.7661	0.3098	0.2181	5.768	66.32	0.6223	0.7110	<u>135.61</u>	
RealSR	SinSR	26.28	0.7347	0.3188	0.2353	6.287	60.80	0.5385	0.6122	135.93
	PiSA-SR	25.50	0.7417	<u>0.2672</u>	0.2044	5.500	70.15	0.6560	0.6702	124.09
	TSD-SR	23.41	0.6886	<u>0.2805</u>	0.2183	5.093	70.77	0.6311	0.7193	114.56
	InvSR	24.13	0.7125	0.2871	0.2123	5.626	68.54	0.6619	0.6790	138.88
	OSEDiff	25.15	0.7341	0.2921	0.2128	5.648	69.09	0.6326	0.6693	123.49
	RCOD _O -Fid.	<u>26.01</u>	0.7427	0.2796	0.2103	5.911	70.25	0.6647	0.6866	121.40
	RCOD _O -Neu.	25.39	0.7264	0.2939	0.2190	5.497	70.34	<u>0.6750</u>	0.7022	127.74
	RCOD _O -Real.	24.62	0.7011	0.3296	0.2375	5.341	<u>70.76</u>	0.6650	0.7084	143.74
	S3Diff	25.18	0.7269	0.2721	<u>0.2005</u>	5.269	67.82	0.6437	0.6727	105.14
	RCOD _S -Fid.	25.42	<u>0.7392</u>	0.2647	0.1976	5.095	69.46	0.6605	0.6509	113.93
	RCOD _S -Neu.	24.78	0.7130	0.2855	0.2073	<u>5.024</u>	70.55	0.6757	0.6886	114.80
	RCOD _S -Real.	24.08	0.6759	0.3228	0.2236	4.900	70.65	0.6719	<u>0.7086</u>	120.00
RCOD _S -Adap.	25.23	0.7313	0.2714	0.2010	5.033	69.72	0.6646	0.6622	<u>112.93</u>	

Table S2: Quantitative comparison with state-of-the-art methods on both synthetic and real-world benchmarks. The best and second best results are highlighted in **bold** and underline, respectively.

2015), MANIQA-pipal (Yang et al. 2022), MUSIQ (Ke et al. 2021), and CLIPIQA (Wang, Chan, and Loy 2023).

Method Comparison: We compare our method with state-of-the-art methods (SOTA) in three categories: multi-step diffusion Real-ISR methods, including StableSR (Wang et al. 2024a), ResShift (Yue, Wang, and Loy 2023), DiffBIR (Lin et al. 2023), and SeeSR (Wu et al. 2024b); one-step diffusion Real-ISR methods, such as SinSR (Wang et al. 2024b), OSEDiff (Wu et al. 2024a), S3Diff (Zhang et al. 2024), TSD-SR (Dong et al. 2025), PiSA-SR (default version) (Sun et al. 2025), and InvSR (Yue, Liao, and Loy 2025); and GAN-based methods, including BSRGAN (Zhang et al. 2021) and Real-ESRGAN (Wang et al. 2021). We quantitatively compare recent SOTA OSD methods in Table S2 on real-world data. **More qualitative comparisons and the full table including synthetic data, multi-step diffusion, and GAN-based methods are in SM.**

Implement Details

Model Setting: To verify our framework, we select two types of recent SOTA OSD Real-ISR methods: OSEDiff (Wu et al. 2024a), which is distilled from a pre-trained

multi-step Stable Diffusion (SD) model, and S3Diff (Zhang et al. 2024), which directly uses SD-T (a distilled version of SD), as our base models. When RCOD is applied to them, they are named RCOD_O and RCOD_S, respectively. The choice of $n = 3$ corresponds to three distinct generation levels in the inference stage: Fidelity, Neutral, and Realism. *i.e.*, $t = 250, 500, \text{ and } 750$ during inference. Since the S3Diff is not directly distilled from a multi-step diffusion, we do not apply DAS on it. RCOD_S-Adap. employs MEM during inference. The input to the MEM in this case is z_L and the features in the last layer degradation estimation model used in (Zhang et al. 2024). The MEM is trained after RCOD_S training, utilizing the same training data. **More details please refer to SM.**

Comparison with State-of-the-Arts

Quantitative Comparisons: We can observe in Table S2: *i)* By applying RCOD, on each dataset, the “-Fid.” versions ($t = 250$) have better full-reference (FR) metrics such as PSNR, SSIM, LPIPS, and FID, while keeping the no-reference (NR) metrics relatively ordinary. In contrast, the “-Real.” versions ($t = 750$) achieve obviously higher NR met-

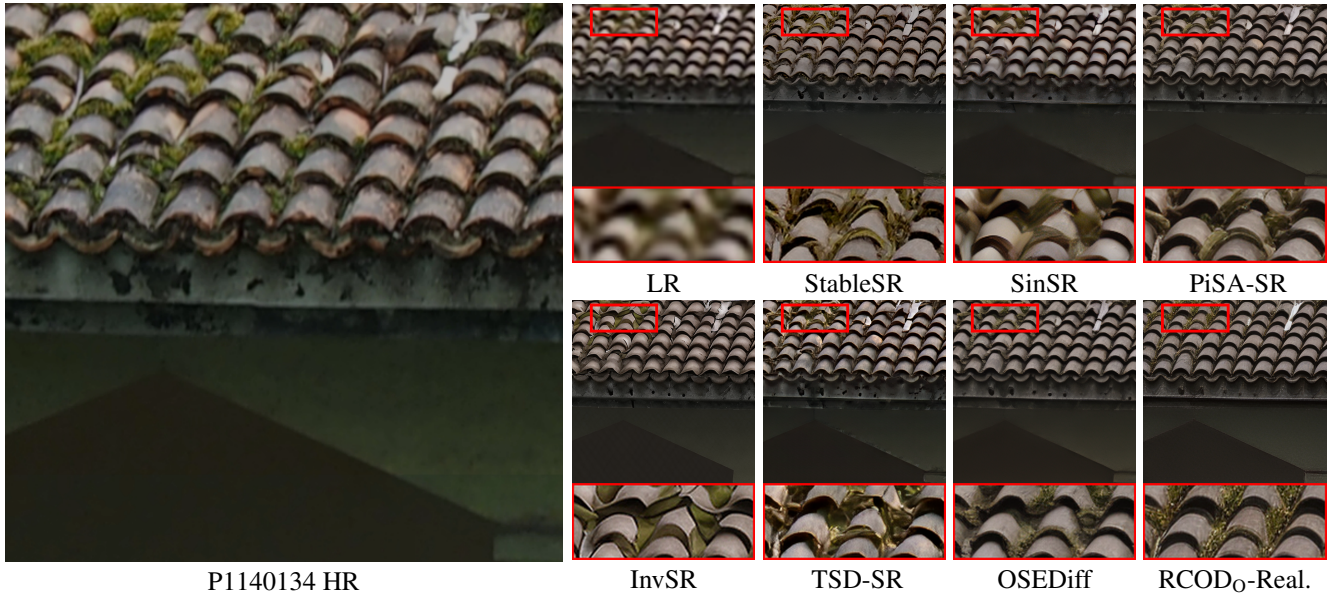


Figure S5: Visual comparison ($\times 4$) of RCOD₀-Real. with other methods on DRealSR data.

rics like MANIQA, MUSIQ, and CLIPQA. Most “-Neu.” versions ($t = 500$) fall within the middle range of the previous two versions. This illustrates that we can effectively and simply control the realism level (usually measured by perceptual NR metrics) during the inference stage, and that the realism level increases monotonically with the timestep. *ii*) RCOD_S-Adap. has relatively balanced metrics between RCOD_S-Fid. and RCOD_S-Neu.. This indicates that most estimated M_L values are closer to 1 than to 0. This roughly matches the cosine similarity value distributions in Fig. S4 (b). *iii*) When applying RCOD, RCOD₀-Fid. and RCOD_S-Adap. perform better than their original methods (OSEDiff and S3Diff, respectively) on most metrics, including PSNR, SSIM, LPIPS, MANIQA, and MUSIQ. Even with a preference for fidelity in FR metrics, RCOD₀-Fid. shows superior performance on some NR metrics, such as MANIQA and MUSIQ, compared to the original OSEDiff method on real-world data. Additionally, RCOD_S-Real. usually achieves the best NR metrics (NIQE and CLIPQA). *iv*) S3Diff shows better performance on the perceptual quality metric DISTS. This may arise from the negative online prompting (NOP) used in training, which provides a more accurate concept of high quality. However, since the text encoder and text prompt are replaced by VPIM in our RCOD_S, the NOP is also removed. Despite this, our RCOD_S-Adap. performs better on other NR metrics.

Time Efficiency: In Table S3, we compare inference time and trainable parameters. All methods are tested on an A100 GPU with a 512×512 input image. RCOD keeps similar time efficiency and trainable parameters as the original methods while have higher PSNR and MANIQA. RCOD₀ even inferences faster as the text extractor is removed.

Qualitative Comparisons: Fig. S5 compares the visual qualities of different Real-ISR methods. RCOD₀-Real. demonstrates its ability to recover more detailed and nat-

ural textures. Fig. S6 illustrates the changes in visual effects as t increases, *i.e.*, from RCOD_S-Fid. ($t = 250$) to RCOD_S-Real. ($t = 750$). As t increases during the inference stage, more skin texture and wrinkles are recovered. RCOD_S-Adap. chooses a proper $t = 500$ in this case, where the M_L range is $[0.5, 0.75]$ according to Eq. 5. The M_L of the LR image (0.621) falls within this range.

Ablation Study We performed a series of ablation studies of the RCOD framework, the details can be found in SM.

Conclusion

We propose RCOD, a framework that enhances one-step diffusion methods for Real-ISR through flexible realism control. RCOD employs latent grouping with degradation-aware sampling during distillation and introduces a robust latent metric enabling denoising networks to assess degradation levels. Applied to two distinct one-step diffusion methods, RCOD achieves superior super-resolution performance across most FR and NR metrics while maintaining computational efficiency. We believe RCOD holds promise for diverse Real-ISR scenarios with varying requirements.

Metrics	PiSA-SR-adj.	OSEDiff	RCOD₀-Fid.	S3Diff	RCOD_S-Adap.
PSNR \uparrow	28.31	27.92	28.90	27.54	27.83
MANIQA \uparrow	0.6156	0.5899	0.6275	0.6134	0.6223
Infer. Time (s)	0.13	0.11	0.09	0.28	0.28
#Trainable Param. (M)	8.1	8.5	9.5	34.5	35.5

Table S3: Efficiency comparison on an NVIDIA A100 GPU. The best results are highlighted in bold.



Figure S6: Visual comparison ($\times 4$) of realism controls during RCOD_S inference stage. The best results are in **bold**.

Supplementary Material for “Realism Control One-step Diffusion for Real-World Image Super-Resolution”

In the supplementary material, we provide the following contents:

- Algorithm Details: Pseudo-code of our RCOD_O training strategy (referring to Section *Methodology* in the main paper).
- Implement Details: Hyper-parameters setting and experimental environments (As a complement to Section *Implement Details* in the main paper).
- Experiments: Full table of quantitative comparisons and more visual Comparisons (as a complement to Section *Experiments* in the main paper).
- Ablation Study (referring to Section *Ablation Study* in the main paper).

Algorithm Details

Pseudo-code The pseudo-code of our RC-OSD training strategy is summarized as Algorithm 1. In inference stage, we do not need to compute M_L . Instead, we directly calculate $\hat{z}_H = F_\theta(z_L; t, c_y)$, where t a user-specified parameter that controls the level of realism for SR output. The choice of t depends on the different application scenarios and is discussed in Subsection “Latent Domain Grouping”.

Implement Details

Training: The training takes over 30k iterations, with a batch size of 4 and a learning rate of $2e^{-5}$. We adopted LoRA for fine-tuning. Follow the original setting (Wu et al. 2024a; Zhang et al. 2024), for RCOD_S, the rank parameter in LoRA is set as 16 for the VAE encoder and 32 for the diffusion UNet, respectively. For RCOD_O, all rank is set to 4.

Hardware and Software Environments: We train and test our model on NVIDIA A100 GPU. The amount of training memory is about 28 GB with batch size 1 using RCOD_O. We use a Linux system with pytorch version 2.4.

Experiments

Quantitative Comparisons: We quantitatively compare recent SOTA SR methods in Table S4 including synthetic and real-world data, multi-step diffusion, and GAN-based methods. Compared with multi-step diffusion methods, our methods demonstrate better NR metrics and perceptual FR metrics across three datasets. Furthermore, their FR fidelity metrics are more competitive with those of multi-step diffusion methods when compared to other OSD methods. On the DrealSR dataset, RCOD_O-Fid. can even surpass some multi-step diffusion methods in many FR metrics (PSNR, SSIM, and LPIPS) and NR metrics (MUSIQ, MANIQA, and CLIP-IQA).

Qualitative Comparisons: We conduct more qualitative comparisons in Fig. S7. On Sony_0049 (DRealSR), RCOD_O-Fid. shows fewer artefacts of handrail than other OSD methods. On Nikon_047 (RealSR) and 0802_pch_00007 (DIV2K), RCOD_O-Real. and RCOD_S-Real. both generate more detailed textures than other OSD methods.

Ablation Study

Effectiveness of VPIM and DAS: To validate the effectiveness of VPIM, we perform ablation studies by replacing the VLM and text encoder (“Text Model”) with VPIM in Table S5 for the “w/o VPIM-Fid.” and “w/o VPIM-Real.” configurations. We observe that both configurations achieve better PSNR, LPIPS, and MANIQA scores than the baseline (the original OSediff). This indicates that VPIM provides not only sufficient semantic information but also fidelity information from LR images. By removing DAS during distillation, as implemented in the “w/o DAS-Fid.” and “w/o DAS-Real.” configurations, we observe that DAS amplifies the performance gap between the fidelity-oriented and realism-oriented configurations. The fidelity-oriented variant achieves higher PSNR and lower LPIPS, while the realism-oriented variant yields higher MANIQA scores—indicating improved realism. This divergence in evaluation metrics demonstrates that DAS effectively enhances LDG’s ability to decouple fidelity preservation from realism generation, enabling finer control over the fidelity–realism trade-off through adaptive timestep regularization.

Choice of n : As mentioned in section “Latent Domain Grouping”, n can only be ≤ 4 . For sufficient flexibility, we

Datasets	Type	Methods	PSNR \uparrow	SSIM \uparrow	LPIPS \downarrow	DISTS \downarrow	NIQE \downarrow	MUSIQ \uparrow	MANIQA \uparrow	CLIPQA \uparrow
DIV2K-Val	Non-Diff.	BSRGAN	24.58	0.6269	0.3351	0.2275	4.752	61.20	0.5071	0.5247
		Real-ESRGAN	24.29	0.6371	0.3112	0.2141	4.679	61.06	0.5501	0.5277
	Multi-step Diff.	StableSR-s200	23.26	0.5726	0.3113	0.2048	4.758	65.92	0.6192	0.6771
		DiffBIR-s50	23.64	0.5647	0.3524	0.2128	4.704	65.81	0.6210	0.6704
		SeeSR-s50	23.68	0.6043	0.3194	0.1968	4.810	68.67	0.6240	0.6936
		PASD-s20	23.14	0.5505	0.3571	0.2207	4.362	68.95	0.6483	0.6788
		ResShift-s15	24.65	0.6181	0.3349	0.2213	6.821	61.09	0.5454	0.6071
	One-step Diff.	SinSR	24.41	0.6018	0.3240	0.2066	6.016	62.82	0.5386	0.6471
		PiSA-SR	23.87	0.6058	0.2823	0.1934	4.550	69.68	0.6400	0.6927
		TSD-SR	22.17	0.5602	0.2736	0.1855	4.340	70.65	0.6077	0.7148
		InvSR	22.90	0.5910	0.5910	0.2058	4.689	68.90	0.6402	0.7181
		OSEDiff	23.72	0.6108	0.2941	0.1976	4.710	67.97	0.6148	0.6683
		RCOD _O -Fid.	24.42	0.6250	0.2858	0.1969	5.041	69.50	0.6433	0.6881
		RCOD _O -Neu.	24.02	0.6147	0.2986	0.2057	4.780	70.21	0.6478	0.7124
		RCOD _O -Real.	23.52	0.5979	0.3285	0.2249	4.655	70.39	0.6332	0.7357
		S3Diff	23.53	0.5933	0.2581	0.1730	4.741	67.92	0.6328	0.7000
		RCOD _S -Fid.	24.06	0.6103	0.2543	0.1869	4.334	68.04	0.6188	0.6515
	RCOD _S -Neu.	23.52	0.5858	0.2894	0.1895	4.243	70.15	0.6358	0.7090	
	RCOD _S -Real.	23.01	0.5574	0.3078	0.2013	4.353	70.75	0.6376	0.7467	
RCOD _S -Adap.	23.72	0.5932	0.2769	0.1880	4.260	69.54	0.6308	0.6936		
DrealSR	Non-Diff.	BSRGAN	28.75	0.8031	0.2883	0.2142	6.519	57.14	0.4878	0.4915
		Real-ESRGAN	28.64	0.8053	0.2847	0.2089	6.693	54.18	0.4907	0.4422
	Multi-step Diff.	StableSR-s200	28.03	0.7536	0.3284	0.2269	6.524	58.51	0.5601	0.6356
		DiffBIR-s50	26.71	0.6571	0.4557	0.2748	6.312	61.07	0.5930	0.6395
		SeeSR-s50	28.17	0.7691	0.3189	0.2315	6.397	64.93	0.6042	0.6804
		PASD-s20	27.36	0.7073	0.3760	0.2531	5.547	64.87	0.6169	0.6808
		ResShift-s15	28.46	0.7673	0.4006	0.2656	8.125	50.60	0.4586	0.5342
	One-step Diff.	SinSR	28.36	0.7515	0.3665	0.2485	6.991	55.33	0.4884	0.6383
		PiSA-SR	28.31	0.7804	0.2960	0.2169	6.200	66.11	0.6156	0.6970
		TSD-SR	25.67	0.7132	0.3538	0.2459	5.991	65.99	0.6327	0.7137
		InvSR	28.33	0.7502	0.3678	0.2481	6.941	55.27	0.4900	0.6385
		OSEDiff	27.92	0.7835	0.2968	0.2165	6.490	64.65	0.5899	0.6963
		RCOD _O -Fid.	28.90	0.7906	0.2919	0.2186	6.817	66.72	0.6275	0.7023
		RCOD _O -Neu.	28.30	0.7775	0.3080	0.2306	6.469	68.03	0.6385	0.7179
		RCOD _O -Real.	27.59	0.7600	0.3389	0.2499	6.172	68.19	0.6295	0.7325
		S3Diff	27.54	0.7491	0.3109	0.2099	6.212	63.94	0.6134	0.7130
		RCOD _S -Fid.	28.09	0.7800	0.3002	0.2149	5.871	65.74	0.6174	0.6963
	RCOD _S -Neu.	27.48	0.7526	0.3256	0.2251	5.636	67.40	0.6339	0.7278	
	RCOD _S -Real.	26.95	0.7190	0.3607	0.2414	5.448	67.58	0.6317	0.7478	
RCOD _S -Adap.	27.83	0.7661	0.3098	0.2181	5.768	66.32	0.6223	0.7110		
RealSR	Non-Diff.	BSRGAN	26.39	0.7654	0.2670	0.2121	5.657	63.21	0.5399	0.5001
		Real-ESRGAN	25.69	0.7616	0.2727	0.2063	5.830	60.18	0.5487	0.4449
	Multi-step Diff.	StableSR-s200	24.70	0.7085	0.3018	0.2288	5.912	65.78	0.6221	0.6178
		DiffBIR-s50	24.75	0.6567	0.3636	0.2312	5.535	64.98	0.6246	0.6463
		SeeSR-s50	25.18	0.7216	0.3009	0.2223	5.408	69.77	0.6442	0.6612
		PASD-s20	25.21	0.6798	0.3380	0.2260	5.414	68.75	0.6487	0.6620
		ResShift-s15	26.31	0.7421	0.3460	0.2498	7.264	58.43	0.5285	0.5444
	One-step Diff.	SinSR	26.28	0.7347	0.3188	0.2353	6.287	60.80	0.5385	0.6122
		PiSA-SR	25.50	0.7417	0.2672	0.2044	5.500	70.15	0.6560	0.6702
		TSD-SR	23.41	0.6886	0.2805	0.2183	5.093	70.77	0.6311	0.7193
		InvSR	24.13	0.7125	0.2871	0.2123	5.626	68.54	0.6619	0.6790
		OSEDiff	25.15	0.7341	0.2921	0.2128	5.648	69.09	0.6326	0.6693
		RCOD _O -Fid.	26.01	0.7427	0.2796	0.2103	5.911	70.25	0.6647	0.6866
		RCOD _O -Neu.	25.39	0.7264	0.2939	0.2190	5.497	70.34	0.6750	0.7022
		RCOD _O -Real.	24.62	0.7011	0.3296	0.2375	5.341	70.76	0.6650	0.7084
		S3Diff	25.18	0.7269	0.2721	0.2005	5.269	67.82	0.6437	0.6727
		RCOD _S -Fid.	25.42	0.7392	0.2647	0.1976	5.095	69.46	0.6605	0.6509
	RCOD _S -Neu.	24.78	0.7130	0.2855	0.2073	5.024	70.55	0.6757	0.6886	
	RCOD _S -Real.	24.08	0.6759	0.3228	0.2236	4.900	70.65	0.6719	0.7086	
RCOD _S -Adap.	25.23	0.7313	0.2714	0.2010	5.033	69.72	0.6646	0.6622		

Table S4: Quantitative comparison with state-of-the-art methods on both synthetic and real-world benchmarks. The best and second best results within both multi-step and one-step diffusion-based methods are highlighted in red and blue, respectively.

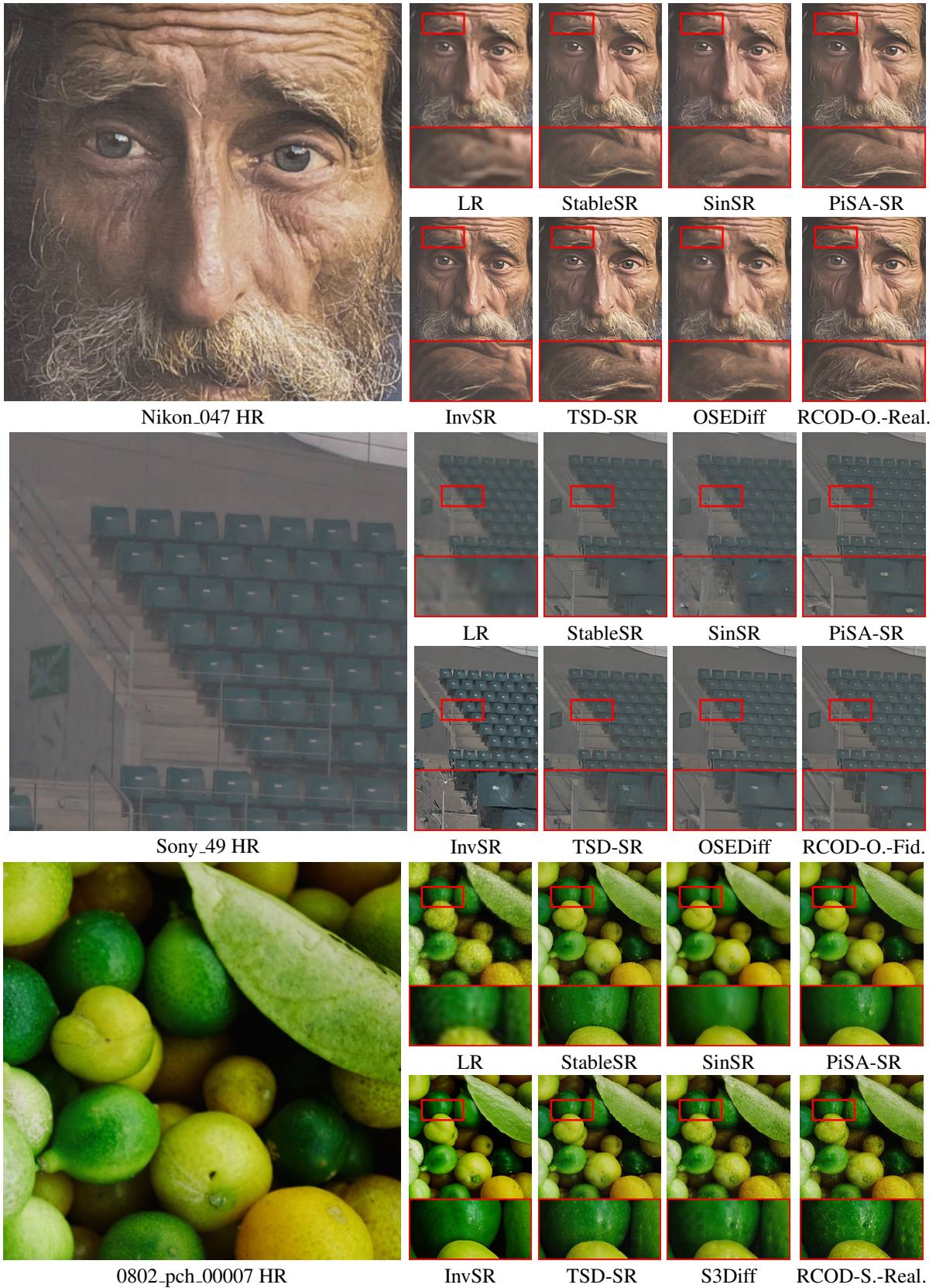


Figure S7: Visual comparison ($\times 4$) on RealSR (Nikon_047), DRealSR (Sony_49), and DIV2K (0802_pch_00007) data.

Algorithm 1: Training Scheme of RCOD_O. Differences from the original OSediff (Wu et al. 2024a) are indicated by a green .

Input: Training dataset \mathcal{S} , pretrained SD parameterized by ϕ , including VAE encoder E_ϕ , latent diffusion network ϵ_θ , and VAE decoder D_ϕ , VPIM Y , training iteration N

```

1 Initialize generator  $G_\theta$  with parameters:  $E_\theta \leftarrow E_\phi$  with trainable LoRA;  $\epsilon_\theta \leftarrow \epsilon_\phi$  with trainable LoRA; fixed parameters  $D_\theta \leftarrow D_\phi$ ; fixed parameters  $Y_\theta \leftarrow Y_\phi$ ; random initialize trainable parameters MLP $_\theta$ 
2 for  $i \leftarrow 1$  to  $N$  do
3   Sample low-resolution image  $\mathbf{x}_L$  and corresponding high-resolution image  $\mathbf{x}_H$  from  $\mathcal{S}$ 
   /* Encode LR and HR images */
4    $(z_L, z_H) \leftarrow E_\theta(\mathbf{x}_L, \mathbf{x}_H)$ 
   /* Acquire degradation-aware visual tokens using VPIM */
5    $c_y \leftarrow Y(\text{MLP}(z_L))$ 
   /* Latent domain grouping */
6    $M_L \leftarrow \text{Equ. (6)}$ ;  $t \leftarrow \text{Equ. (5)}$ 
   /* Denoising and decoding */
7    $\hat{z}_H \leftarrow F_\theta(z_L; c_y, t)$ ;  $\hat{\mathbf{x}}_H \leftarrow D_\theta(\hat{z}_H)$ 
   /* Data consistency loss */
8    $\mathcal{L}_{\text{data}} \leftarrow \mathcal{L}_{\text{MSE}}(\hat{\mathbf{x}}_H, \mathbf{x}_H) + \lambda_1 \mathcal{L}_{\text{LPIPS}}(\hat{\mathbf{x}}_H, \mathbf{x}_H)$ 
   /* regularization with degradation-aware sampling */
9   Sample noise  $\epsilon \sim \mathcal{N}(0, I)$ 
10  Sample  $t_r$  according to Equ. (7)
11   $\hat{z}_t \leftarrow \alpha_{t_r} \hat{z}_H + \sigma_{t_r} \epsilon$ ;  $z_\phi \leftarrow \text{stopgrad}(F_\phi(\hat{z}_t; c_y))$ ;  $z_{\phi'} \leftarrow \text{stopgrad}(F_{\phi'}(\hat{z}_t; c_y))$ ;  $\omega \leftarrow 1/\text{mean}(\|z_\phi - \hat{z}_H\|)$ ;  $\mathcal{L}_{\text{reg}} \leftarrow \omega \|z_{\phi'} - z_\phi\|$ 
   /* Regularizer fine-tuning loss */
12  Sample noise  $\epsilon \sim \mathcal{N}(0, I)$ 
13  Sample  $t$  from  $\{1, \dots, T\}$   $z_t \leftarrow \alpha_t \cdot \text{stopgrad}(\hat{z}_H) + \sigma_t \epsilon$ 
14   $\mathcal{L}_{\text{diff}} \leftarrow \mathcal{L}_{\text{MSE}}(\epsilon_{\phi'}(z_t; t, c_y), \epsilon)$ 
   /* Total loss and update */
15   $\mathcal{L}_{\text{total}} \leftarrow \mathcal{L}_{\text{data}} + \lambda_2 \mathcal{L}_{\text{reg}} + \lambda_3 \mathcal{L}_{\text{diff}} + \lambda_4 \mathcal{L}_{\text{cls}}$  Update  $\theta$  using  $\mathcal{L}_{\text{total}}$ ; update  $\phi'$  using  $\mathcal{L}_{\text{diff}}$ 
16 end

```

Output: Trained generator G_θ

consider $n \geq 3$. Therefore, we compare the training results for $n = 3$ and $n = 4$ in Table S6. We find that RCOD_O-Real. ($n = 4$) performs much worse than RCOD_O-Real. ($n = 3$). To explain this phenomenon, we visualize the training data distribution for the two choices in Fig. S8. We observe that there is too little data for training at large t (when M_L is small). Thus, we finally choose $n = 3$ for our experiment.

Robustness of M_L : Due to the encoder of the VAE being trainable in most SD-based method settings, we consider a domain shift phenomenon during training: the distribution of M_L may change after training. Therefore, we compare the M_L values of the entire training dataset before and after training in main manuscript Fig. 4 (b). The histogram shows a slight shift in the metric, with values becoming closer to larger similarities, but the overall distribution remains similar. This indicates that even though the model aligns the feature domains of LR and HR, M_L retains its robustness in measuring the divergence in the latent domain.

Correlation of M_L and image quality: In Table 1(b) in main manuscript, we calculate $|\text{Spearman coefficient}| \uparrow$ of different M_L and image quality metrics (which are calculated by LR and HR images). Fig. S9 visualize the correlation of randomly selected 600 points. We can find that cosine similarity exhibits a higher correlation coefficient with image quality metrics compared to other distances.

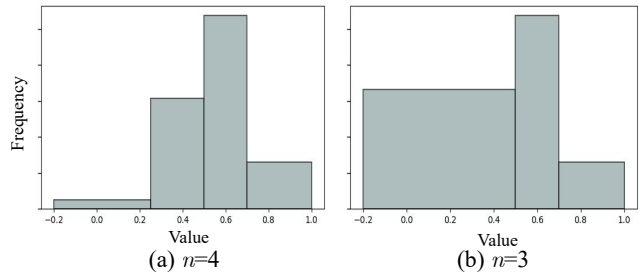


Figure S8: Distribution of (a) mean value of LR and HR training images in the latent domain, (b) the M_L metric in the latent domain of VAE before and after training.

References

- Agustsson, E.; and Timofte, R. 2017. Ntire 2017 challenge on single image super-resolution: Dataset and study. In *CVPRW*, 126–135.
- Cai, J.; Zeng, H.; Yong, H.; Cao, Z.; and Zhang, L. 2019. Toward real-world single image super-resolution: A new benchmark and a new model. In *ICCV*, 3086–3095.
- Chen, B.; Li, G.; Wu, R.; Zhang, X.; Chen, J.; Zhang, J.; and Zhang, L. 2025. Adversarial diffusion compression for real-world image super-resolution. In *CVPR*, 28208–28220.
- Chen, J.; Pan, J.; and Dong, J. 2025. Faithdiff: Unleashing diffusion priors for faithful image super-resolution. In *CVPR*, 28188–28197.

	LDG	VPIM	Text Model	DAS	PSNR \uparrow	LPIPS \downarrow	MANIQA \uparrow
Baseline	×	×	✓	×	25.15	0.2921	0.6326
w/o VPIM-Fid.	✓	×	✓	×	25.99	0.2824	0.6541
w/o VPIM-Real.	✓	×	✓	×	24.23	0.3242	0.6642
w/o LDG	×	✓	×	×	25.34	0.2877	0.6320
w/o DAS-Fid.	✓	✓	×	×	25.90	0.2806	0.6553
w/o DAS-Real.	✓	✓	×	×	24.89	0.3275	0.6602
RCOD_O-Fid.	✓	✓	×	✓	26.01	0.2796	0.6647
RCOD_O-Real.	✓	✓	×	✓	24.62	0.3296	0.6650

Table S5: Ablation study of modules. The best results are highlighted in bold.

	PSNR \uparrow	DISTS \downarrow	LPIPS \downarrow	MANIQA \uparrow
RCOD _O -Fid. ($n = 4$)	26.00	0.2111	0.2805	0.6490
RCOD _O -Fid. ($n = 3$)	26.01	0.2103	0.2796	0.6647
RCOD _O -Real. ($n = 4$)	24.02	0.2590	0.3588	0.6400
RCOD _O -Real. ($n = 3$)	24.62	0.2375	0.3296	0.6650

Table S6: Ablation study of grouping strategy. The best results are highlighted in bold.

Chen, T.; Kornblith, S.; Norouzi, M.; and Hinton, G. 2020. A simple framework for contrastive learning of visual representations. In *ICML*, 1597–1607.

Ding, K.; Ma, K.; Wang, S.; and Simoncelli, E. P. 2020. Image quality assessment: Unifying structure and texture similarity. *IEEE PAMI*, 44(5): 2567–2581.

Dong, C.; Loy, C. C.; He, K.; and Tang, X. 2015. Image super-resolution using deep convolutional networks. *IEEE transactions on pattern analysis and machine intelligence*, 38(2): 295–307.

Dong, L.; Fan, Q.; Guo, Y.; Wang, Z.; Zhang, Q.; Chen, J.; Luo, Y.; and Zou, C. 2025. Tsd-sr: One-step diffusion with target score distillation for real-world image super-resolution. In *CVPR*, 23174–23184.

Ho, J.; Jain, A.; and Abbeel, P. 2020. Denoising diffusion probabilistic models. In *NeurIPS*.

Hu, E. J.; Shen, Y.; Wallis, P.; Allen-Zhu, Z.; Li, Y.; Wang, S.; Wang, L.; and Chen, W. 2022. Lora: Low-rank adaptation of large language models. In *ICLR*.

Ignatov, A.; Kobyshev, N.; Timofte, R.; Vanhoey, K.; and Van Gool, L. 2017. Dslr-quality photos on mobile devices with deep convolutional networks. In *ICCV*.

Ji, X.; Cao, Y.; Tai, Y.; Wang, C.; Li, J.; and Huang, F. 2020. Real-world super-resolution via kernel estimation and noise injection. In *CVPRW*.

Karras, T.; Laine, S.; and Aila, T. 2019. A style-based gen-

erator architecture for generative adversarial networks. In *CVPR*.

Ke, J.; Wang, Q.; Wang, Y.; Milanfar, P.; and Yang, F. 2021. Musiq: Multi-scale image quality transformer. In *ICCV*.

Kim, J.; Kwon Lee, J.; and Mu Lee, K. 2016. Accurate image super-resolution using very deep convolutional networks. In *CVPR*.

Ledig, C.; Theis, L.; Huszár, F.; Caballero, J.; Cunningham, A.; Acosta, A.; Aitken, A.; Tejani, A.; Totz, J.; Wang, Z.; et al. 2017. Photo-realistic single image super-resolution using a generative adversarial network. In *CVPR*, 4681–4690.

Li, Y.; Zhang, K.; Liang, J.; Cao, J.; Liu, C.; Gong, R.; Zhang, Y.; Tang, H.; Liu, Y.; Demandolx, D.; et al. 2023. Lsdrr: A large scale dataset for image restoration. In *CVPR*, 1775–1787.

Liang, J.; Cao, J.; Sun, G.; Zhang, K.; Van Gool, L.; and Timofte, R. 2021. Swinir: Image restoration using swin transformer. In *ICCV*.

Lin, X.; He, J.; Chen, Z.; Lyu, Z.; Fei, B.; Dai, B.; Ouyang, W.; Qiao, Y.; and Dong, C. 2023. Diffbir: Towards blind image restoration with generative diffusion prior. *arXiv preprint arXiv:2308.15070*.

Liu, A.; Liu, Y.; Gu, J.; Qiao, Y.; and Dong, C. 2022. Blind image super-resolution: A survey and beyond. *IEEE PAMI*, 45(5): 5461–5480.

Meng, C.; Rombach, R.; Gao, R.; Kingma, D.; Ermon, S.;

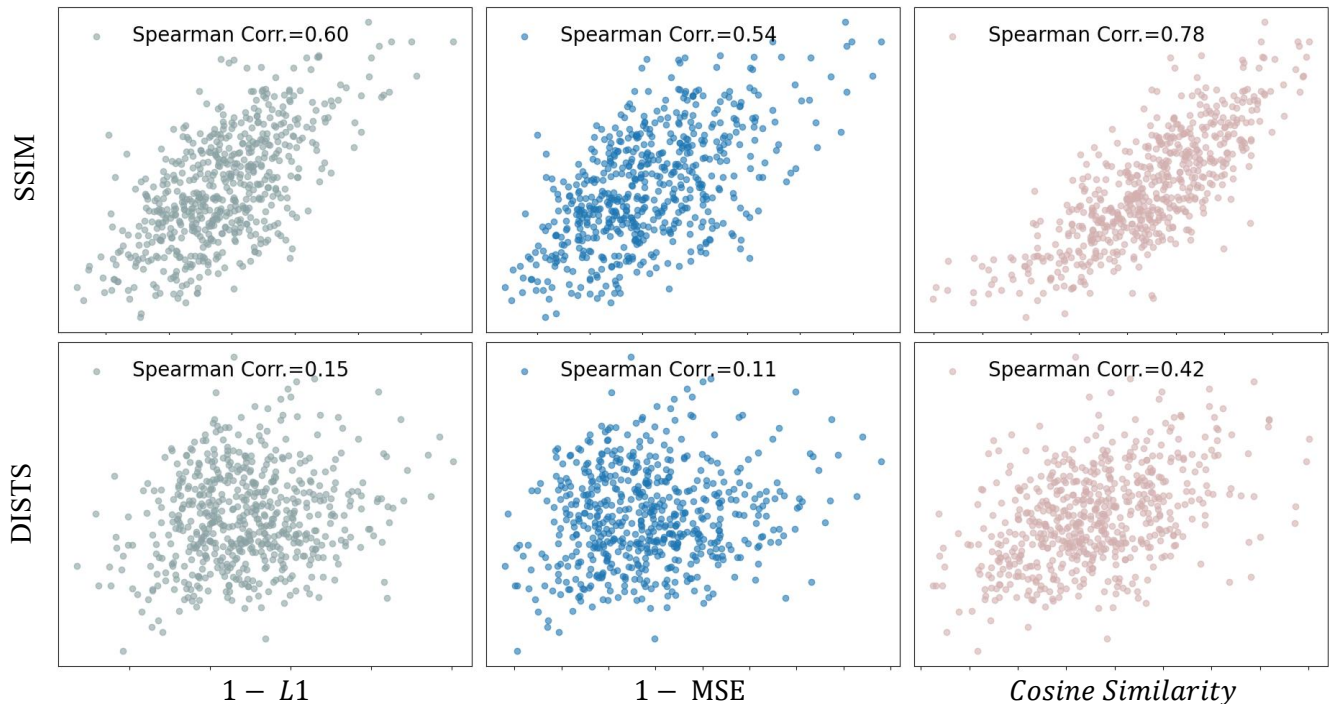


Figure S9: Visualization of $|\text{Spearman coefficient}| \uparrow$ of different M_L distances and image quality metrics.

Ho, J.; and Salimans, T. 2023. On distillation of guided diffusion models. In *CVPR*, 14297–14306.

Nguyen, T. H.; and Tran, A. 2024. Swiftbrush: One-step text-to-image diffusion model with variational score distillation. In *CVPR*.

Rombach, R.; Blattmann, A.; Lorenz, D.; Esser, P.; and Ommer, B. 2022. High-resolution image synthesis with latent diffusion models. In *CVPR*, 10684–10695.

Salimans, T.; and Ho, J. 2022. Progressive distillation for fast sampling of diffusion models. *arXiv preprint arXiv:2202.00512*.

Song, Y.; Dhariwal, P.; Chen, M.; and Sutskever, I. 2023. Consistency models. In *ICML*.

Song, Y.; Sohl-Dickstein, J.; Kingma, D. P.; Kumar, A.; Ermon, S.; and Poole, B. 2020. Score-based generative modeling through stochastic differential equations. *arXiv preprint arXiv:2011.13456*.

Sun, L.; Wu, R.; Ma, Z.; Liu, S.; Yi, Q.; and Zhang, L. 2025. Pixel-level and semantic-level adjustable super-resolution: A dual-lora approach. In *Proceedings of the Computer Vision and Pattern Recognition Conference*, 2333–2343.

Wang, J.; Chan, K. C.; and Loy, C. C. 2023. Exploring clip for assessing the look and feel of images. In *AAAI*, volume 37, 2555–2563.

Wang, J.; Yue, Z.; Zhou, S.; Chan, K. C.; and Loy, C. C. 2024a. Exploiting diffusion prior for real-world image super-resolution. *International Journal of Computer Vision*, 1–21.

Wang, X.; Xie, L.; Dong, C.; and Shan, Y. 2021. Real-esrgan: Training real-world blind super-resolution with pure synthetic data. In *ICCV*.

Wang, Y.; Yang, W.; Chen, X.; Wang, Y.; Guo, L.; Chau, L.-P.; Liu, Z.; Qiao, Y.; Kot, A. C.; and Wen, B. 2024b. SinSR: Diffusion-Based Image Super-Resolution in a Single Step. In *CVPR*.

Wang, Z.; Bovik, A. C.; Sheikh, H. R.; and Simoncelli, E. P. 2004. Image quality assessment: from error visibility to structural similarity. *IEEE TIP*, 13(4): 600–612.

Wang, Z.; Lu, C.; Wang, Y.; Bao, F.; Li, C.; Su, H.; and Zhu, J. 2024c. Prolificdreamer: High-fidelity and diverse text-to-3d generation with variational score distillation. In *NeurIPS*.

Wei, P.; Xie, Z.; Lu, H.; Zhan, Z.; Ye, Q.; Zuo, W.; and Lin, L. 2020. Component divide-and-conquer for real-world image super-resolution. In *ECCV*, 101–117. Springer.

Wu, R.; Sun, L.; Ma, Z.; and Zhang, L. 2024a. One-step effective diffusion network for real-world image super-resolution. *NeurIPS*, 37: 92529–92553.

Wu, R.; Yang, T.; Sun, L.; Zhang, Z.; Li, S.; and Zhang, L. 2024b. Seesr: Towards semantics-aware real-world image super-resolution. In *CVPR*.

Yang, S.; Wu, T.; Shi, S.; Lao, S.; Gong, Y.; Cao, M.; Wang, J.; and Yang, Y. 2022. Maniqa: Multi-dimension attention network for no-reference image quality assessment. In *CVPR*, 1191–1200.

Yin, T.; Gharbi, M.; Park, T.; Zhang, R.; Shechtman, E.; Durand, F.; and Freeman, W. T. 2024a. Improved Distribution Matching Distillation for Fast Image Synthesis. *arXiv preprint arXiv:2405.14867*.

Yin, T.; Gharbi, M.; Zhang, R.; Shechtman, E.; Durand, F.; Freeman, W. T.; and Park, T. 2024b. One-step diffusion with distribution matching distillation. In *CVPR*, 6613–6623.

Yue, Z.; Liao, K.; and Loy, C. C. 2025. Arbitrary-steps image super-resolution via diffusion inversion. In *CVPR*, 23153–23163.

Yue, Z.; Wang, J.; and Loy, C. C. 2023. Resshift: Efficient diffusion model for image super-resolution by residual shifting. In *NeurIPS*.

Zhang, A.; Yue, Z.; Pei, R.; Ren, W.; and Cao, X. 2024. Degradation-guided one-step image super-resolution with diffusion priors. *arXiv preprint arXiv:2409.17058*.

Zhang, K.; Liang, J.; Van Gool, L.; and Timofte, R. 2021. Designing a practical degradation model for deep blind image super-resolution. In *ICCV*, 4791–4800.

Zhang, L.; Rao, A.; and Agrawala, M. 2023. Adding conditional control to text-to-image diffusion models. In *ICCV*, 3836–3847.

Zhang, L.; Zhang, L.; and Bovik, A. C. 2015. A feature-enriched completely blind image quality evaluator. *IEEE TIP*, 24(8): 2579–2591.

Zhang, R.; Isola, P.; Efros, A. A.; Shechtman, E.; and Wang, O. 2018a. The unreasonable effectiveness of deep features as a perceptual metric. In *CVPR*, 586–595.

Zhang, Y.; Li, K.; Li, K.; Wang, L.; Zhong, B.; and Fu, Y. 2018b. Image super-resolution using very deep residual channel attention networks. In *ECCV*.

Zhu, Y.; Wang, R.; Lu, S.; Li, J.; Yan, H.; and Zhang, K. 2024. Oftsr: One-step flow for image super-resolution with tunable fidelity-realism trade-offs. *arXiv preprint arXiv:2412.09465*.